Journal of Applied Physics

RESEARCH ARTICLE | MARCH 22 2024

Thermally generated magnonic spin currents in a polycrystalline gadolinium iron garnet thin film with perpendicular magnetic anisotropy

Amit Chanda ; Christian Holzmann ; Noah Schulz ; David Stein ; Manfred Albrecht ; Manh-Huong Phan ; Hariharan Srikanth

J. Appl. Phys. 135, 123901 (2024)
https://doi.org/10.1063/5.0188568

AIP Publishing

Journal of Applied Physics ARTICLE pubs.aip.org/aip/jap

Thermally generated magnonic spin currents in a polycrystalline gadolinium iron garnet thin film with perpendicular magnetic anisotropy

Cite as: J. Appl. Phys. **135**, 123901 (2024); doi: 10.1063/5.0188568
Submitted: 18 January 2024 · Accepted: 5 March 2024 ·
Published Online: 22 March 2024

View Online Export Citation CrossMark

Amit Chanda,[1,a)] Christian Holzmann,[2] Noah Schulz,[1] David Stein,[2] Manfred Albrecht,[2] Manh-Huong Phan,[1] and Hariharan Srikanth[1,a)]

AFFILIATIONS

[1]Department of Physics, University of South Florida, Tampa, Florida 33620, USA
[2]Institute of Physics, University of Augsburg, Augsburg 86159, Germany

[a)]**Authors to whom correspondence should be addressed:** achanda@usf.edu and sharihar@usf.edu

ABSTRACT

Rare-earth iron garnets (REIGs) are the benchmark systems for magnonics, including the longitudinal spin Seebeck effect (LSSE). While most research has focused on single-crystalline REIGs on complimentary garnet substrates, moving to more, cost-effective complementary metal-oxide semiconductor (CMOS)-compatible substrates is important to integrate REIG thin films with existing technology. In this regard, we grow a 130 nm-thick polycrystalline gadolinium iron garnet (GdIG) film on the Si/SiO_2 substrate and investigate the temperature-dependent LSSE. Interestingly, the polycrystalline GdIG film exhibits perpendicular magnetic anisotropy (PMA) at room temperature which is induced by tensile in-plane (IP)-strain originating from the thermal-expansion mismatch between the GdIG film and the substrate during rapid thermal annealing. Further, a spin-reorientation transition from the out-of-plane IP direction below $T_S = 180$ K is observed. Additionally, the film reveals a magnetic compensation temperature, T_{Comp}, of ≈240 K. The LSSE voltage not only demonstrates a sign-inversion around T_{Comp}, but also shows noticeable changes around T_S. As compared to a single-crystalline GdIG film, the lower LSSE voltage for the polycrystalline GdIG is attributed to the higher effective magnetic anisotropy and enhanced magnon scattering at the grain boundaries. Our study not only paves the way for the cost-effective growth of CMOS-compatible REIG-based systems with PMA for magnonic memory and information processing applications, but also highlights the fact that the spincaloritronic and spin-insulatronic properties of the polycrystalline REIGs follow those of their single-crystalline counterparts with reduced spin-to-charge conversion efficiency through LSSE which can be tuned further by controlling the average gran size and interface engineering.

I. INTRODUCTION

In recent years, rare-earth iron garnet (REIG) based ferrimagnetic insulators have attracted immense attention primarily due to their tunable magnetic properties, ultrafast magnetization dynamics, and low-losses in the terahertz (THz) regime.[1–4] $Y_3Fe_5O_{12}$ (YIG) has been an extensively explored REIG for generating and transmitting pure spin currents due to its ultra-low Gilbert damping.[5] Although YIG films typically exhibit an in-plane (IP) easy axis, REIG films with perpendicular magnetic anisotropy (PMA) are of considerable interest in spin-based-electronics for their promising efficiency in spin–orbit-torque driven magnetization switching, current-driven dynamics induced by chiral magnetic textures, domain-wall based high-density information storage, etc.[6–8] PMA can be induced in single-crystalline epitaxial REIG films by choosing a complimentary garnet substrate whose magnetoelastic anisotropy is positive and large enough to overcome the shape anisotropy.[9–13] However, for practical spintronic applications based on REIGs, it is necessary to grow REIG films on complementary metal-oxide semiconductor (CMOS)-compatible non-garnet substrates without destroying the most significant and desirable materials characteristics, such as PMA.[14–16] Previous studies indicate that it is possible to grow polycrystalline REIGs with PMA on non-garnet substrates when the thermal-expansion mismatch between the REIG films and the non-garnet substrate promotes the desired PMA.[14,17,18]

The study of the excitation, propagation, manipulation, and detection of spin waves, known as magnonics, has gained significant attention due to its potential for applications in the development of high-performance, low-noise-level, and low-dissipation magnetic-storage and information processing devices.[1,19,20] Within the vast field of magnonics, the longitudinal spin Seebeck effect (LSSE) provides an efficient route for the thermal-generation of incoherent THz magnonic excitations in a magnetic insulator parallel to the direction of an applied temperature gradient and transmission of the thermally generated magnonic spin current to an adjacent heavy metal layer that converts the spin current into detectable charge current through the inverse spin Hall effect (ISHE).[21,22] YIG is considered as a benchmark system for the LSSE.[21,23] However, recently, an interesting member of the REIG family, $Gd_3Fe_5O_{12}$ (GdIG), has been reported to exhibit an exhilarating spincaloritronic property: the magnonic spin current induced by LSSE can be efficiently manipulated solely by tuning the compensation temperature which is in sharp contrast to that observed in YIG.[24–28] GdIG is a compensated ferrimagnetic insulator wherein the weak antiferromagnetic exchange coupling between the Gd^{3+} and Fe^{3+} sublattices and strong temperature sensitivity of the Gd^{3+} sublattice magnetization give rise to a magnetic compensation close to room temperature.[24] The LSSE voltage in GdIG/Pt bilayers shows a sign-inversion around this magnetic compensation independent of the GdIG film thickness and substrate-choice.[27] A recent study reported the existence of PMA at room temperature in single-crystalline GdIG thin films grown on $Gd_3Sc_2Ga_3O_{12}$ (GSGG) substrates, however, the magnetic easy axis reorients from the out-of-plane (OOP) to the IP direction at low temperatures due to the competition between the weakly temperature-dependent magnetoelastic anisotropy and the strongly temperature-dependent shape anisotropy.[12] Polycrystalline GdIG films[29,30] were reported to exhibit magnetic compensation, but neither PMA nor any trace of temperature-driven spin reorientation has been realized in those polycrystalline GdIG films. Therefore, the effects of PMA and spin reorientation on the LSSE and its temperature evolution in the polycrystalline GdIG films have not been investigated so far. From another perspective, combining cost-effective CMOS-compatible substrates with PMA will expand applications of REIG thin films in magnonic memory and information processing. To address this, in this report, we have explored (1) the existence of PMA as well as the temperature-driven spin reorientation in a 130 nm-thick polycrystalline GdIG film grown on a Si/SiO_2 substrate and (2) the thermal-generation of pure magnonic spin currents in the polycrystalline GdIG film and the influences of magnetic compensation and spin reorientation on it. For brevity, the polycrystalline Si/SiO_2/GdIG(130 nm)/Pt(5 nm) film is denoted as *p*-GdIG. In this context, we recall that LSSE voltage decreases with decreasing magnetic film thickness.[23,31,32] Since the LSSE signal for a polycrystalline film is usually much weaker compared to its single-crystalline counterpart with comparable thickness,[33–35] we compared the LSSE voltage for our *p*-GdIG film with a thinner single-crystalline GdIG film with similar magnetic properties, for which we chose a 31 nm-thick single-crystalline GdIG film grown epitaxially on a (111)-oriented GSGG substrate. For brevity, the single-crystalline GSGG/GdIG(31 nm)/Pt(5 nm) film is denoted as *s*-GdIG in this manuscript.

II. EXPERIMENTAL DETAILS

The *p*-GdIG film was grown by pulsed laser deposition (PLD) using a KrF excimer laser with a wavelength of 248 nm, at a fluence of 3–4 J/cm at room temperature, with a repetition rate of 3 Hz and an oxygen background pressure of 0.004 mbar. Re-crystallization of the film was achieved by post-deposition rapid thermal annealing at 800 °C for 3 min in a mixture of about 25% O_2 and 75% N_2, using a heating-rate of about 150 K/s. The *s*-GdIG film was also grown by PLD at a laser-repletion rate of 2 Hz, resulting in a growth rate of 0.01–0.02 nm/s, a substrate temperature of 595 °C, and an oxygen partial-pressure of 0.05 mbar. After the deposition, the substrate was cooled-down to room temperature at 5 K/min, maintaining the oxygen atmosphere. A 5 nm-thick Pt layer was deposited on the GdIG films at room temperature *ex situ* by DC magnetron-sputtering using a shadow mask. The GdIG films were annealed at 400 °C for 1h inside the sputter-chamber prior to the Pt deposition. The structural properties of the thin films were characterized by x-ray diffraction (XRD) using a Cu Kα source, and their surface morphology was investigated by atomic force microscopy (AFM). Different orientations of the grains in the *p*-GdIG film were further characterized by scanning electron microscopy (SEM), using an electron acceleration voltage of 20 kV, and a backscattered electron detector at a sample analysis angle of 70°, analyzing electron backscatter diffraction patterns (EBSD). The magnetic properties of the *p*-GdIG film were measured using a superconducting quantum interference device-vibrating sample magnetometer (SQUID-VSM). For the LSSE measurements, we employed a custom-built setup that utilizes a universal PPMS sample-puck. The *p*-GdIG film was sandwiched between two copper plates during the measurements as displayed in Fig. 5(a). Single layers of Kapton-tape were attached to the bare surfaces of the top (cold) and bottom (hot) copper plates to ensure electrical insulation between the copper plates and film surfaces, and Apiezon N-grease was used to ensure a good thermal-connectivity between the film-surface and the Kapton-tapes. A resistive chip-heater (PT-100 RTD sensor) and a calibrated Si-diode thermometer (DT-621-HR Si-diode sensor) were attached to each of the copper plates using GE varnish. The heaters and thermometers attached to the copper plates were connected to two separate temperature controllers (Scientific Instruments Model No. 9700). A temperature gradient along the *z*-direction between the hot and cold copper plates was established by individually controlling the temperatures of both these plates. The LSSE voltage generated along the *y*-direction across the Pt layer was recorded by a Keithley 2182a nanovoltmeter while sweeping an IP DC magnetic field produced by the superconducting magnet of the PPMS along the *x*-direction. The Ohmic contacts for the LSSE voltage measurements were made by attaching a pair of ultra-thin gold wires (25 μm diameter) to the Pt layer by high quality conducting silver paint (SPI Supplies). A more detailed description of our experimental setup can be found elsewhere.[27,36]

III. RESULTS

Figure 1(a) shows the AFM image of the *p*-GdIG film. Micrometer-sized polycrystalline grains are visible for *p*-GdIG with a low root-mean-square (RMS)-roughness of 0.4 nm for the individual grains. The XRD $\theta - 2\theta$ diffractogram for the *p*-GdIG film [Fig. 1(b)] measured at gracing incidence with an angle of 5° shows

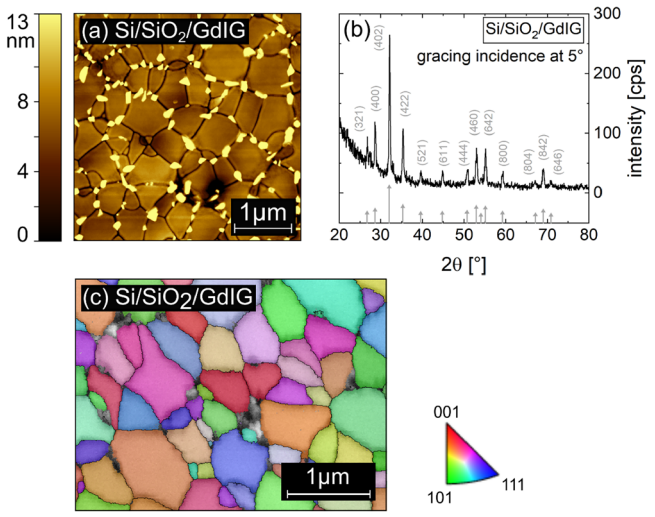

FIG. 1. (a) AFM image for the *p*-GdIG thin film. (b) The gracing incidence diffraction of the *p*-GdIG film. (c) EBSD image for the *p*-GdIG film, showing IPF coloring along the OOP direction.

garnet peaks with no evidence of a preferred crystallographic orientation or any non-garnet phase. The film crystal-orientation is reconstructed from EBSD Kikuchi patterns, and Fig. 1(c) shows the identified garnet grain-orientation in inverse pole-figure (IPF) coloring along the OOP direction. While all grains are identified as garnet phase, the film shows a polycrystalline structure with random grain-orientations. The *s*-GdIG film exhibits a similar RMS-roughness of 0.4 nm.[27] The AFM and XRD $\theta - 2\theta$ diffractogram revealing the (444) planes of the *s*-GdIG film are presented in Fig. S1 in the supplementary material. The sharp Bragg reflection associated with the GSGG substrate is noticeable at 50.28°, whereas the Bragg (444) peak associated with the GdIG film is visible at a higher angle than the bulk-GdIG reflection indicating compressive OOP-stress of the film.

Figure 2(a) displays the magnetic field-dependent magnetization, $M(H)$ at 300 K measured in the IP and OOP configurations on the *p*-GdIG film. Clearly, the *p*-GdIG film exhibits OOP magnetic easy axis at 300 K. The effective magnetic anisotropy of a (111)-oriented single-crystalline garnet film has contributions from magnetic shape anisotropy (K_{shape}), cubic magneto-crystalline anisotropy (K_{mc}), and magnetoelastic anisotropy (K_{me}),[9,12,37] i.e.,

$$K_{eff} = K_{shape} + K_{mc} + K_{me} = -\frac{1}{2}\mu_0 M_S^2 - \frac{K_1}{12} - \frac{3}{2}\lambda_{111}\left(\frac{\gamma}{1+\nu}\right)F,$$

where Y, ν, and λ_{111} are Young's modulus, Poisson's ratio, and magnetostriction coefficient along the [111]-direction, respectively, M_S is the saturation magnetization, and

$$F = \left[\frac{a_{GSGG} - a_{GdIG}}{a_{GSGG}}\right]$$

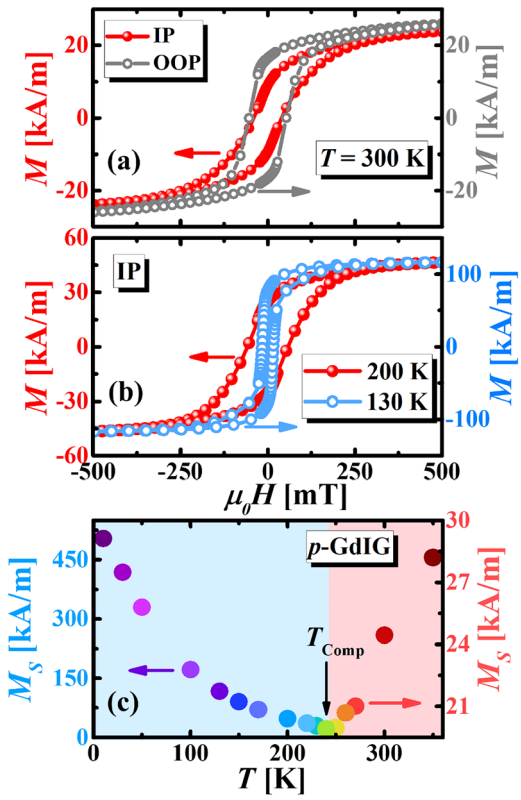

FIG. 2. (a) IP and OOP $M(H)$ at 300 K for the *p*-GdIG film. (b) IP $M(H)$ at 200 and 130 K for the *p*-GdIG film. (c) *T*-dependence of M_S for the *p*-GdIG film.

is the lattice-mismatch. However, for a polycrystalline garnet film, K_{mc} can be neglected and K_{eff} can be expressed as[14,17]

$$K_{eff} = K_{shape} + K_{me} = -\frac{1}{2}\mu_0 M_S^2 - \frac{3}{2}\lambda_{avg}\left(\frac{E}{1-\nu}\right)\Delta\alpha_T \delta T,$$

where λ_{avg} is the approximate average of the magnetostriction-coefficients λ_{100} and λ_{111}, $\Delta\alpha_T$ is the difference in thermal-expansion coefficients (α_T) between the garnet film and the substrate, δT is the temperature difference between the annealing-temperature and room temperature, and E is the elastic modulus. Considering $\delta T = 770$ K, $\lambda_{avg} = -1.9 \times 10^6$, $\alpha_{GdIG} = 2 \times 10^{-5}$,[38] $\alpha_{Si/SiO_2} = 3 \times 10^{-6}$,[39] and $\Delta\alpha_T = 1.7 \times 10^{-5}$, we obtain $K_{me} \approx 10$ kJ/m^3. Furthermore, considering $M_S \approx 25$ kA/m at room temperature, we obtain $K_{shape} = -0.4$ kJ/m^3 and hence, $K_{eff} = K_{shape} + K_{me} = +9.6$ kJ/m^3, clearly confirming PMA for the *p*-GdIG film at room temperature. Therefore, for the *p*-GdIG film, the tensile IP strain originating from the thermal-expansion mismatch between the GdIG film and the substrate leads to the dominating contribution of K_{me} toward K_{eff}, and hence PMA.[14,17] Notably, the theoretical value of K_{eff} for our *p*-GdIG film at room temperature is nearly six times higher than that of a single-crystalline GdIG film of comparable thickness with PMA grown under tensile IP strain on the GSGG

substrate.[12] Furthermore, the coercivity of our *p*-GdIG film is higher than that of the single-crystalline GSGG/GdIG film of similar thickness,[12] which is expected as the magnetic anisotropy field is typically higher for a polycrystalline film than a single-crystal film due to greater strain-state.[14,17] Additionally, the grain boundaries in the polycrystalline film act as domain-wall pinning centers and lead to higher coercivity.[14,17]

Figure 2(b) depicts the IP $M(H)$ loops at 200 and 130 K for the *p*-GdIG film. Evidently, the magnetic easy axis of this film reorients from the high temperature OOP direction to the low temperature IP direction at $T_S \approx 180$ K. Similar behavior was also observed for single-crystalline GdIG films grown under tensile IP strain on the GSGG substrate.[12] The temperature dependence of M_S obtained from the IP $M(H)$ for the *p*-GdIG film is shown in Fig. 2(c). Evidently, M_S first decreases with decreasing temperature from 300 K, vanishes at the magnetic compensation temperature (T_{Comp}), and then increases significantly upon further decreasing temperature. The drastic enhancement of M_S at low temperature is caused by the strong increase in the *c*-site Gd^{3+} sublattice magnetization together with the *a*-site Fe^{3+} sublattice magnetization, which overcomes the *d*-site Fe^{3+} sublattice magnetization.[24,26,27] We found T_{Comp} of ≈240 K for the *p*-GdIG film. The appearance of a spin-reorientation transition in the *p*-GdIG film at T_S can be attributed to the dominating contribution of K_{shape} toward K_{eff} at low temperatures due to enhanced M_S at low-T which overcomes the effect of K_{me}.[12] The detailed magnetic properties of the *s*-GdIG film are demonstrated in Fig. S2 in the supplementary material. It is evident from Fig. S2 in the supplementary material that the *s*-GdIG film also shows PMA at room temperature and a low temperature spin-reorientation transition at $T_S = 180$ K. However, the magnetic compensation in *s*-GdIG occurs at a somewhat reduced temperature of $T_{Comp} \approx 225$ K. In this context, we would like to highlight that the *s*-GdIG films are saturated at sufficiently low magnetic fields and the GSGG substrate is paramagnetic. Therefore, the high field $M(H)$ signal (typically for $H > 500$ mT) was fitted by a linear trend, which was in turn used to subtract the linear paramagnetic substrate signal from the $M(H)$ data.

We have also performed anomalous Hall Effect (AHE) measurements on the *p*-GdIG film as it has an OOP magnetic easy axis at room temperature. In REIG/heavy metal (HM) bilayer heterostructures, the AHE signal is dominated by the spin Hall anomalous Hall effect (SH-AHE),[40,41] which is an interfacial spin-dependent transport phenomena driven by ISHE and SHE induced spin-to-charge interconversion. Therefore, it is expected that the temperature evolution of SH-AHE signal would show significant changes around the magnetic compensation.

In Figs. 3(a) and 3(b), we show the magnetic field dependence of the anomalous Hall resistance, $R_{xy}^{AHE}(H)$ above ($190\ K \leq T \leq 300\ K$) and below ($130\ K \leq T \leq 190\ K$) the spin-reorientation transition temperature, T_S. Clearly, $R_{xy}^{AHE}(H)$ shows a well-defined square-shaped hysteresis loop at room temperature, indicating good PMA of our *p*-GdIG film. For a clearer visualization, we have plotted $R_{xy}^{AHE}(H)$ hysteresis loops at temperatures $T = 300$ and 130 K on the left *y* axis and the IP $M(H)$ loops measured at the same temperatures on the right *y* axis, in Figs. 3(c) and 3(d), respectively. It is evident from these data that the *p*-GdIG film has OOP magnetic easy axis at room temperature but switches to an IP magnetic easy axis at $T = 130$ K, supporting the observations of prominent PMA at room temperature and strong IP magnetic easy axis below the spin-reorientation transition. The magnitude of the background-corrected anomalous Hall resistance

$$|R_{xy}^{AHE}| = \frac{R_{xy}^{AHE}(+\mu_0 H_{sat}) - R_{xy}^{AHE}(-\mu_0 H_{sat})}{2}$$

decreases with lowering temperature from 300 K and becomes negligibly small when the magnetic compensation is approached, as shown in Fig. 3(e). The R_{xy}^{AHE} signal changes its polarity and its absolute value enhances with further decreasing the temperature below the magnetic compensation at T_{Comp} but shows a prominent decrease below the spin reorientation at T_S. In other words, the sign of the SH-AHE signal is negative above T_{Comp} and positive below the T_{Comp}, like what was observed in compensated single-crystalline REIGs GdIG/Pt,[42] $Tb_3Fe_5O_{12}$/Pt,[10,43] etc. Note that the interfacial exchange coupling between the REIG and Pt is the governing factor for the spin-angular momentum transfer between the REIG and Pt layers and hence for the R_{xy}^{AHE} signal.[43] Previous studies indicate that the interfacial exchange coupling between the REIG and Pt layers is ferromagnetic for the YIG/Pt,[44,45] $Tb_3Fe_5O_{12}$/Pt,[43] and $Tm_3Fe_5O_{12}$/Pt[43] systems which is primarily governed by the exchange interaction between the Fe^{3+} sublattice and Pt. In the case of GdIG/Pt bilayers, the magnetic moment of Gd^{3+} ion originates from the 4*f*-orbital which is more localized than the 3*d*-orbitals of the Fe^{3+} ions.[42] Hence, the spin-angular momentum transfer between the GdIG and Pt bilayers is predominantly governed by the interfacial exchange interaction between the *d*-site Fe^{3+} sublattice magnetization and Pt layer at room temperature rather than the exchange interaction between the *c*-site Gd^{3+} sublattice magnetization and Pt.[42] Note that the orientations of all the sublattice magnetizations are reversed below the T_{Comp} in the GdIG/Pt bilayer. Furthermore, the Gd^{3+} sublattice magnetization increases radically at low temperatures and overcomes the *d*-site Fe^{3+} sublattice magnetization.[27] Therefore, the interfacial exchange coupling between the GdIG and Pt bilayers has significant contribution from the exchange interaction between the Gd^{3+} sublattice magnetization and the Pt layer in addition to the predominant exchange interaction *d*-site Fe^{3+} sublattice magnetization and the Pt layer below the T_{Comp}. While the interfacial exchange interaction between the *d*-site Fe^{3+} sublattice and the Pt layer remains ferromagnetic at low temperatures,[43] an antiferromagnetic exchange interaction is expected between the Gd^{3+} sublattice and the Pt layer below the T_{Comp}.[46] Since the *c*-site Gd^{3+} and *d*-site Fe^{3+} sublattice magnetizations are antiferromagnetically aligned at all temperatures,[24,27] both the aforementioned interfacial exchange interactions tend to align the electron spins in the Pt layer along the same direction below the T_{Comp}. Hence, the direction of polarization of the electron spins in Pt is reversed accordingly which eventually leads to opposite polarity of the SH-AHE signal below the T_{Comp} (see Fig. 4). It is also noteworthy that the coercivity of the $R_{xy}^{AHE}(H)$ loop increases as the T_{Comp} is approached and decreases with further lowering temperature below the T_{Comp}, which is consistent with what was observed in the single-crystalline GdIG films with PMA.[42,47]

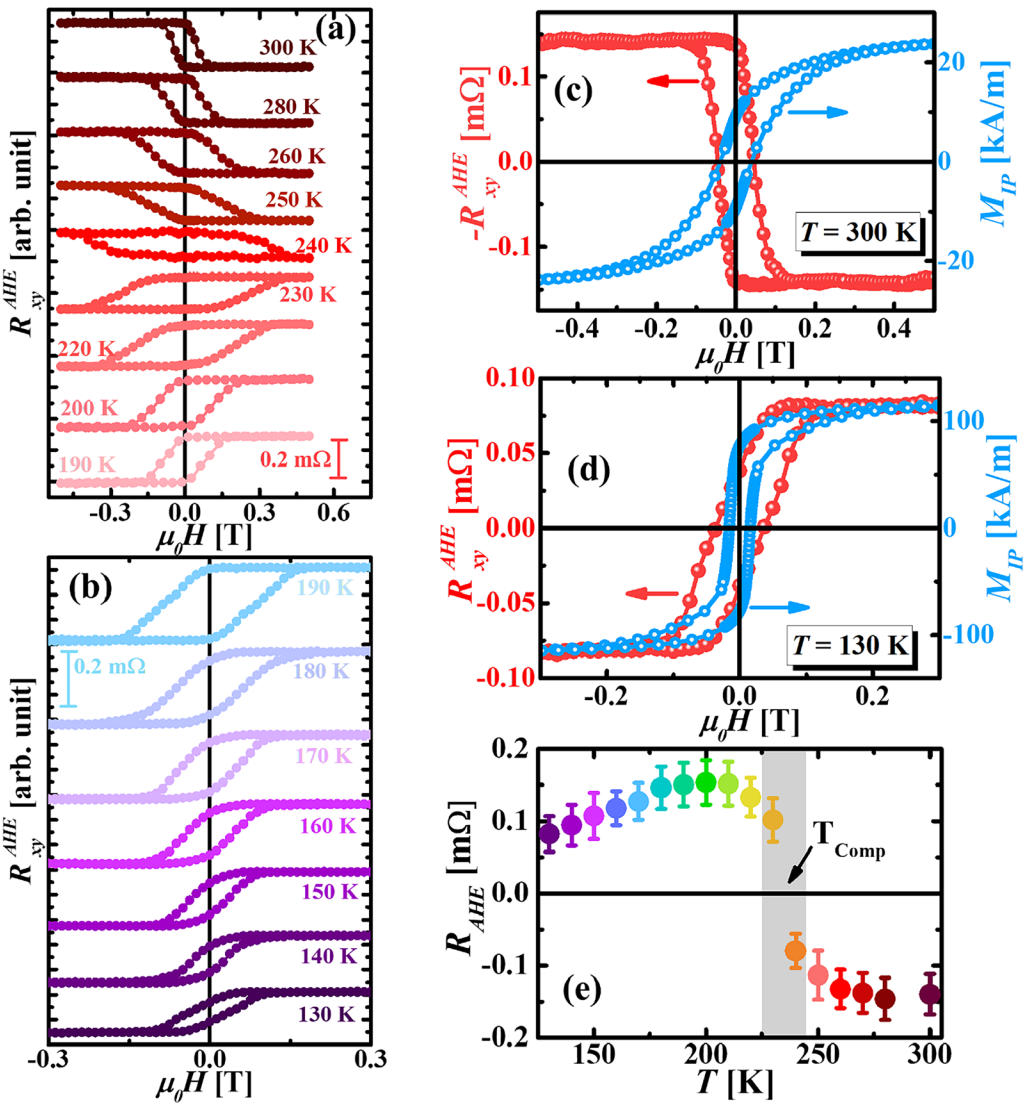

FIG. 3. $R^{AHE}_{xy}(H)$ hysteresis loops for the *p*-GdIG film in the temperature ranges: (a) 190 K $\leq T \leq$ 295 K and (b) 130K $\leq T \leq$ 190K. $R^{AHE}_{xy}(H)$ hysteresis loops at temperatures: (c) T = 300 and (d) 130 K on the left *y* axis and the IP $M(H)$ loops measured at the same temperatures on the right *y* axis, respectively. (e) Temperature dependence of the background-corrected anomalous Hall resistance, $|R^{AHE}_{xy}|$, for the *p*-GdIG film.

Next, we demonstrate the thermo-spin transport in the *p*-GdIG film. Figure 5(a) represents the schematic-illustration of our LSSE measurement configuration. Simultaneous application of a OOP (*z*-direction) temperature gradient ($\overrightarrow{\nabla T}$) and an IP (*x*-direction) DC magnetic field across the film gives rise to diffusion of thermally generated magnons and establishes a spatial-gradient of magnon-accumulation in the GdIG layer along the direction of $\overrightarrow{\nabla T}$ (*z*-direction).[48] The accumulated magnons near the GdIG/Pt interface injects a spin current, $\overrightarrow{J_S} \propto -S_{LSSE}\overrightarrow{\nabla T}$ to the adjacent Pt layer along the *z*-direction, where S_{LSSE} is the LSSE coefficient.[48,49] The injected spin current is converted into a charge current, $\overrightarrow{J_C} = \left(\frac{2e}{\hbar}\right)\theta^{Pt}_{SH}(\overrightarrow{J_S} \times \overrightarrow{\sigma_S})$ in the Pt layer along the *y*-direction via the inverse spin Hall effect (ISHE), where e, $\hbar$, θ^{Pt}_{SH}, and $\overrightarrow{\sigma_S}$ are the electronic-charge, the reduced Planck's constant, the spin Hall angle of Pt, and the spin-polarization vector, respectively. The corresponding LSSE voltage is expressed as[48,50,51]

$$V_{LSSE} = R_y L_y D_{Pt}\left(\frac{2e}{\hbar}\right)\theta^{Pt}_{SH}|J_S|\tanh\left(\frac{t_{Pt}}{2D_{Pt}}\right), \quad (1)$$

where R_y, L_y, D_{Pt}, and t_{Pt} represent the resistance between the contact-leads, the distance between the contact-leads (≈3 mm), the

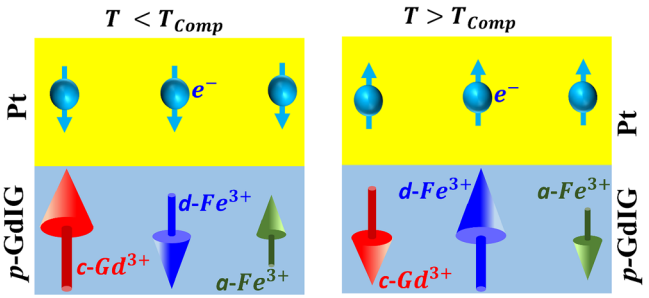

FIG. 4. Schematic illustrations demonstrating the orientations of the sublattice magnetizations of the GdIG film and the direction of spin polarizations of the electron spins in the Pt layer above and below the magnetic compensation at T_{Comp}.

spin-diffusion length of Pt, and the Pt layer thickness (5 nm), respectively.

Figure 5(c) display the H-dependence of the ISHE voltage, $V_{ISHE}(H)$ for the p-GdIG film for different temperature differences between the hot (T_{hot}) and cold (T_{cold}) plates, $\Delta T = (T_{hot} - T_{cold})$, at a fixed average sample-temperature $T = \frac{T_{hot}+T_{cold}}{2} = 295$ K. For all ΔT, $V_{ISHE}(H)$ mimics the corresponding $M(H)$ loops.[27] Evidently, $V_{ISHE}(H)$ for the p-GdIG film increases with increasing ΔT. Figure 5(d) demonstrates the ΔT-dependence of the background-corrected LSSE voltage

$$V_{LSSE}(\Delta T) = \left[\frac{V_{ISHE}(+\mu_0 H_{sat},\ \Delta T) - V_{ISHE}(-\mu_0 H_{sat},\ \Delta T)}{2}\right]$$

for the p-GdIG film, where $\mu_0 H_{sat}$ is the saturation field. Notably, V_{LSSE} increases linearly with ΔT.[27] Figure 6(a) displays the $V_{ISHE}(H)$ hysteresis loops for the p-GdIG film in the temperature range of 190 K $\leq T \leq$ 295 K for $\Delta T = +15$ K. Clearly, the $V_{ISHE}(H)$ loop for the p-GdIG film changes its sign below the T_{Comp}. Furthermore, the $V_{ISHE}(H)$ signal decreases approaching T_{Comp} but enhances again below T_{Comp}. The sign-reversal of $V_{ISHE}(H)$ in the GdIG film in the vicinity of T_{Comp} is caused by the reversal of the sublattice magnetizations.[24,25,27,52] To understand the nature of thermo-spin transport around $T_S = 180$ K, we display the $V_{ISHE}(H)$ hysteresis loops for the p-GdIG film in the temperature

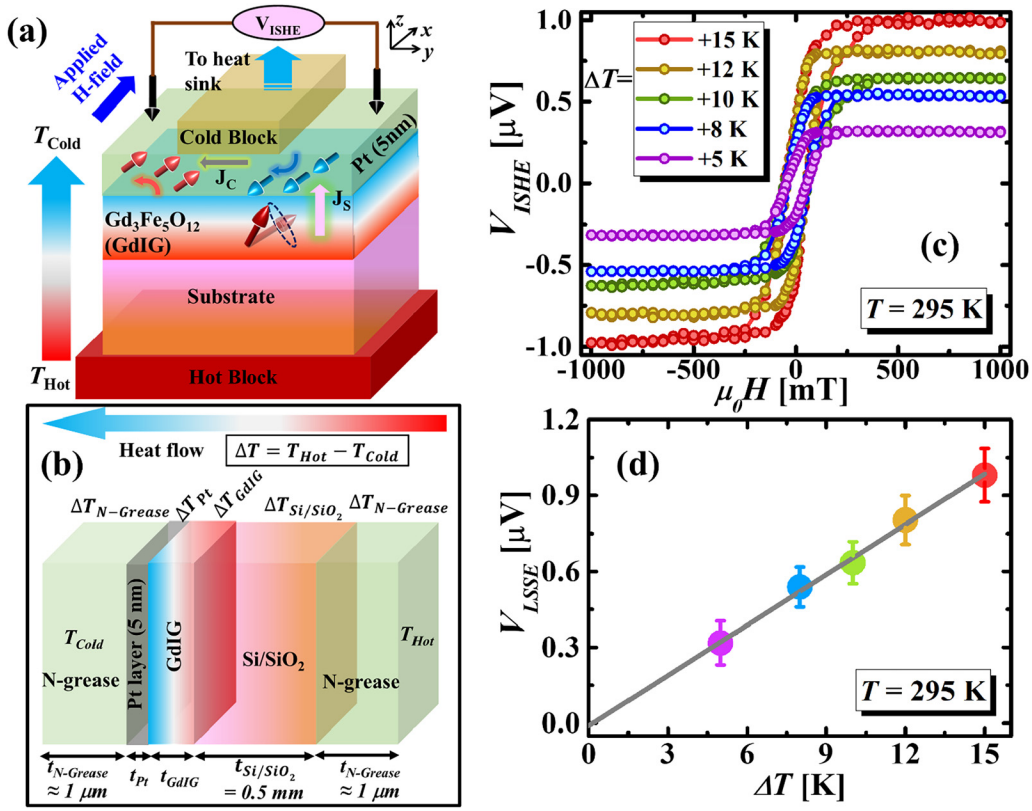

FIG. 5. (a) The schematic-illustration of our LSSE measurement configuration, (b) schematic representation of the heat flow across the substrate/GdIG/Pt heterostructure, and (c) $V_{ISHE}(H)$ loops for the p-GdIG film for different values of ΔT at 295 K. (d) Linear fit to the ΔT-dependence of the background-corrected LSSE voltage, $V_{LSSE}(\Delta T)$ for the p-GdIG film.

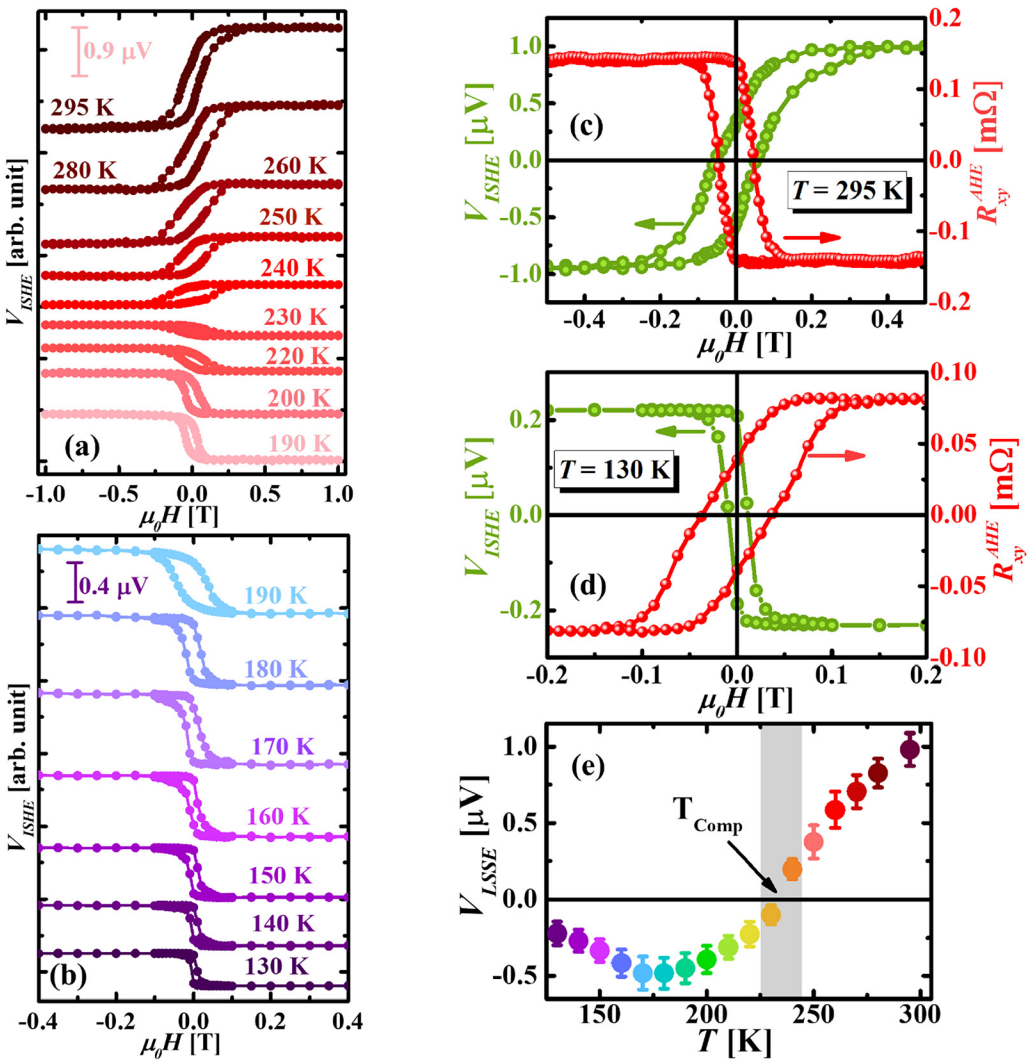

FIG. 6. $V_{ISHE}(H)$ hysteresis loops for the *p*-GdIG film in the temperature ranges: (a) 190 K $\leq T \leq$ 295 K and (b) 130 K $\leq T \leq$ 190 K for $\Delta T = +15$ K. $V_{ISHE}(H)$ hysteresis loops at temperatures (c) $T = 295$ and (d) 130 K on the left *y* axis and corresponding $R_{xy}^{AHE}(H)$ loops measured at the same temperatures on the right *y* axis, respectively. (e) Temperature dependence of the background-corrected LSSE voltage, V_{LSSE} for the *p*-GdIG film.

range: 130 K $\leq T \leq$ 190 K for $\Delta T = +15$ K in Fig. 6(b). The $V_{ISHE}(H)$ signal strength decreases gradually with decreasing temperature, especially below T_S.

To obtain a clearer picture of the influences of PMA and the spin-reorientation transition on the LSSE signal, we have plotted the $V_{ISHE}(H)$ hysteresis loops at temperatures $T = 295$ and 130 K on the left *y* axis and the corresponding $R_{xy}^{AHE}(H)$ hysteresis loops on the right *y* axis, in Figs. 6(c) and 6(d), respectively. Note that the $V_{ISHE}(H)$ hysteresis loops were obtained while sweeping an IP magnetic field whereas $R_{xy}^{AHE}(H)$ hysteresis loops were recorded while scanning an OOP magnetic field. Therefore, these observations clearly suggest that the $V_{ISHE}(H)$ hysteresis loops follow the corresponding IP $M(H)$ hysteresis loops. In other words, the $V_{ISHE}(H)$ hysteresis loops are strongly influenced by the PMA at room temperature and spin-reorientation transition at low temperatures. In Fig. 6(e), we display the temperature dependence of $V_{LSSE}(T, \mu_0 H_{sat})$ for the *p*-GdIG film. Clearly, V_{LSSE} is positive for $T \geq T_{Comp}$ but becomes negative for $T < T_{Comp}$. Furthermore, $V_{LSSE}(T)$ increases below T_{Comp} and shows a minimum around T_S which is followed by gradual decrease at low temperatures.

For an effective estimation of the temperature dependence of the LSSE coefficient (S_{LSSE}) of our *p*-GdIG film, the contributions of the thermal resistances of the substrate (Si/SiO_2) and the N-grease layers as well as the interfacial thermal resistances need to

be considered.[53] According to Jimenez-Cavero *et al.*,[54] the total temperature difference (ΔT) across the substrate/GdIG/Pt heterostructure can be expressed as a linear combination of temperature drops in the Pt layer, at the Pt/GdIG interface, in the GdIG layer, at the GdIG/substrate interface, across the Si/SiO_2 substrate as well as in the N-grease layers (thickness $\approx 1\,\mu$m) on both sides of the substrate/GdIG/Pt heterostructure, and hence can be expressed as[54]

$$\Delta T = \Delta T_{\mathrm{Pt}} + \Delta T_{\frac{\mathrm{Pt}}{\mathrm{GdIG}}} + \Delta T_{\mathrm{GdIG}} + \Delta T_{\frac{\mathrm{GdIG}}{\mathrm{Substrate}}} + \Delta T_{\mathrm{Substrate}} + 2\Delta T_{\mathrm{N-Grease}},$$

as shown in Fig. 5(b). Since the thermal resistance of Pt is very small compared to the other contributions and the bulk contributions toward the measured ISHE voltage dominate over the interfacial contributions when the thickness of the magnetic layer (*p*-GdIG) is high enough,[54] the total temperature difference can be approximately written as, $\Delta T = \Delta T_{\mathrm{GdIG}} + \Delta T_{\mathrm{Substrate}} + 2 \cdot \Delta T_{\mathrm{N-Grease}}$. In the steady state, the effective temperature difference across the GdIG film can be written as[55]

$$\Delta T_{\mathrm{eff}} = \Delta T_{\mathrm{GdIG}} = \frac{\Delta T}{\left[1 + \frac{\kappa_{\mathrm{GdIG}}}{t_{\mathrm{GdIG}}}\left(\frac{2t_{\mathrm{N-Grease}}}{\kappa_{\mathrm{N-Grease}}} + \frac{t_{\mathrm{Substrate}}}{\kappa_{\mathrm{Substrate}}}\right)\right]}. \quad (2)$$

Here, $t_{\mathrm{N-Grease}}$, t_{GdIG}, and t_{GdIG} are the thicknesses of the N-grease layers, the substrate, and the GdIG layer, respectively, and $\kappa_{\mathrm{N-Grease}}$, κ_{GdIG}, and $\kappa_{\mathrm{Substrate}}$ are the thermal conductivities of the grease layers, the GdIG layer, and the substrate, respectively. Using the reported values of κ_{GdIG}, $\kappa_{\mathrm{Substrate}}$(κ_{Si}), and $\kappa_{\mathrm{N-Grease}}$ from the literature,[56–59] we determined ΔT_{eff} for our *p*-GdIG film at different temperatures. Here, we have ignored the interfacial thermal resistances between the N-grease and the hot/cold plates as well as between the sample and N-grease layers.[36] It is important to note that because of the polycrystalline nature, the thermal conductivity of our *p*-GdIG film ($\kappa^{\mathrm{Poly}}_{\mathrm{GdIG}}$) is lower than that of a single-crystalline GdIG film ($\kappa^{\mathrm{Single}}_{\mathrm{GdIG}}$). As shown by Miura *et al.*,[60] the thermal conductivity of single-crystalline YIG is higher than that of the polycrystalline YIG over a broad temperature range. However, this difference in thermal conductivity is large at low temperatures (below 100 K), but comparatively smaller at higher temperatures. Therefore, for our measured temperature range, we have assumed that $\kappa^{\mathrm{Poly}}_{\mathrm{GdIG}} \approx \kappa^{\mathrm{Single}}_{\mathrm{GdIG}} = \kappa_{\mathrm{GdIG}}$. Figure 7(a) shows the temperature variation of $\Delta T_{\mathrm{eff}} = \Delta T_{\mathrm{GdIG}}$ for our *p*-GdIG film estimated using Eq. (2). Using the temperature dependence of ΔT_{eff}, we have estimated the temperature dependence of the LSSE coefficient,

$$S_{\mathrm{LSSE}} = \left(\frac{V_{\mathrm{LSSE}} \cdot L_z}{\Delta T_{\mathrm{eff}} \cdot L_y}\right),$$

for our *p*-GdIG film (L_z is the thickness of our *p*-GdIG film = 130 nm), as demonstrated in Fig. 7(b). Clearly, the trend of $S_{\mathrm{LSSE}}(T)$ is quite similar to that of $V_{\mathrm{LSSE}}(T)$ for our *p*-GdIG film.

IV. DISCUSSION

Now let us discuss about the origin of the decrease in V_{LSSE} at low temperatures in our *p*-GdIG film. It is known that V_{LSSE} for single-crystalline GdIG is reported to undergo a second sign-inversion at about 80 K which originates from two competing magnon modes: a Gd^{3+}-moment dominated uniform-precession mode in the GHz regime (α-mode) and a Fe^{3+}-moment dominated gapped, optical mode (β-mode).[24,25,27,52] At low temperatures, the contribution of the α-mode overcomes that of the β-mode giving rise to a sign-inversion of V_{LSSE} below 80 K. Therefore, the gradual decrease of $|V_{\mathrm{LSSE}}|$ and hence, $|S_{\mathrm{LSSE}}|$ in our *p*-GdIG/Pt film at low temperatures is associated with the competition between α and β-modes. For the β-mode, the magnon energy gap ($\hbar\omega_M$) at $k = 0$ increases at low temperatures due to the enhanced Gd^{3+}-sublattice magnetization.[24] Furthermore, K_{me} and hence, K_{eff} increases drastically at low temperatures.[12,61,62] Since $\hbar\omega_M \propto 2K_{\mathrm{eff}}$,[32,63] and $|V_{\mathrm{LSSE}}|$ of GdIG is dominated by the β-mode within our measured temperature range,[24] the appearance of the minimum in $V_{\mathrm{LSSE}}(T)$ and the gradual decrease in $|V_{\mathrm{LSSE}}|$ below $\approx$180 K is associated with the magnetic anisotropy that governs $\hbar\omega_M$ of the β-mode. Previous studies on LSSE in single-crystalline GdIG/Pt bilayers also indicated a sharp-increase followed by a rapid decrease in $|V_{\mathrm{LSSE}}|$ below their respective T_{Comp}.[24,25,27,52] However, in those studies, GdIG films were grown on GGG substrates and hence, they showed an IP easy axis throughout the measured temperature range without any spin reorientation. For our case, the *p*-GdIG film shows PMA at high temperatures and spin-reorientation transition followed by IP

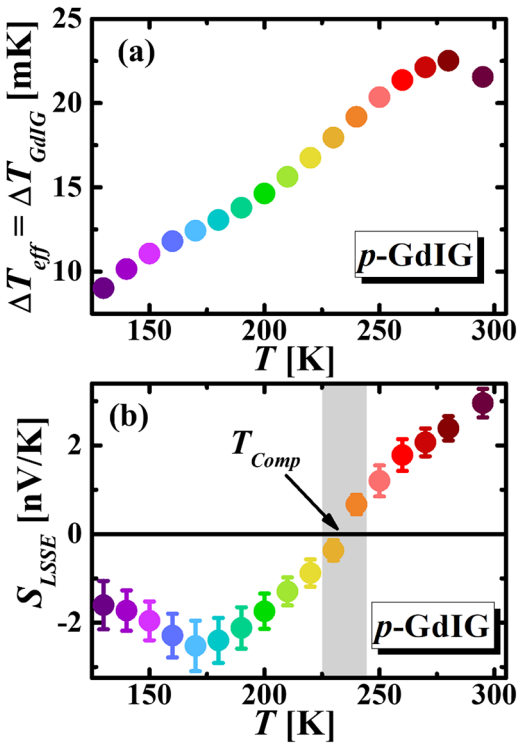

FIG. 7. (a) Temperature variation of $\Delta T_{\mathrm{eff}} = \Delta T_{\mathrm{GdIG}}$ for our *p*-GdIG film estimated using Eq. (2). (b) Temperature dependence of the LSSE coefficient, $S_{\mathrm{LSSE}} = (V_{LSSE}.L_z/\Delta T_{\mathrm{eff}}.L_y)$, for our *p*-GdIG film.

easy axis below T_S. Note that the magnon propagation length, $\langle\xi\rangle \propto \frac{1}{\sqrt{K_{\text{eff}}}}$.[32,63] The GdIG films do not have any preferred magnetic easy axis at T_S, and hence, K_{eff} becomes very small, which leads to large $\langle\xi\rangle$ and hence, $|V_{\text{LSSE}}|$ and hence, $|S_{\text{LSSE}}|$ shows a maximum. Therefore, the occurrences of the minimum in both $V_{\text{LSSE}}(T)$ and $S_{\text{LSSE}}(T)$ in our *p*-GdIG film are associated with the change in K_{eff} around T_S caused by the spin reorientation which influences $\hbar\omega_M$ of the β-modes.

Next, we compare the V_{LSSE} signal for our *p*-GdIG film with the single-crystalline GdIG film. Figures 8(a) and 8(b) compare the $V_{\text{ISHE}}(H)$ hysteresis loops for the *p*-GdIG and *s*-GdIG films at 295 and 190 K, respectively for $\Delta T = +15$ K, which clearly indicate that the LSSE signal in the *s*-GdIG film is higher than that in the *p*-GdIG film. The $V_{\text{ISHE}}(H)$ hysteresis loops for the *s*-GdIG film at different temperatures for fixed $\Delta T = +15$ K and $V_{\text{LSSE}}(T)$ are shown in Fig. S3 in the supplementary material. It is evident that $|V_{\text{LSSE}}|$ is higher in the *s*-GdIG film than in the *p*-GdIG film at all temperatures. To quantify the difference in $|V_{\text{LSSE}}|$ between a single-crystalline and a polycrystalline GdIG film of comparable thicknesses, we recall an atomistic spin model that connects V_{LSSE} with the magnetic layer thickness (t) and $\langle\xi\rangle$ through a phenomenological expression,[23,31,32] $V_{\text{LSSE}}(t) \propto \left[1 - e^{-\frac{t}{\langle\xi\rangle}}\right]$. Considering, $\langle\xi\rangle \approx 45 \pm 8$ nm for single-crystalline GdIG films at 295 K,[64] and $V_{\text{LSSE}} \approx 1350 \pm 150$ nV for GSGG/GdIG(31 nm)/Pt(5 nm) at 295 K, we estimate the approximated value of V_{LSSE} of a 130 nm single-crystalline GdIG film as ≈2545 ± 150 nV, which is nearly 2.5-times larger than that of the 130 nm *p*-GdIG film at 295 K ($V_{\text{LSSE}} \approx 980 \pm 106$ nV). Furthermore, the *p*-GdIG film shows larger coercive-field and magnetic anisotropy field compared to the *s*-GdIG film possibly because of the higher strain-state and domain-wall pinning at the grain boundaries in *p*-GdIG.[14,17] Higher magnetic anisotropy in *p*-GdIG enhances $\hbar\omega_M$,[32,63] which leads to only high-frequency thermal magnon propagation with shorter $\langle\xi\rangle$.

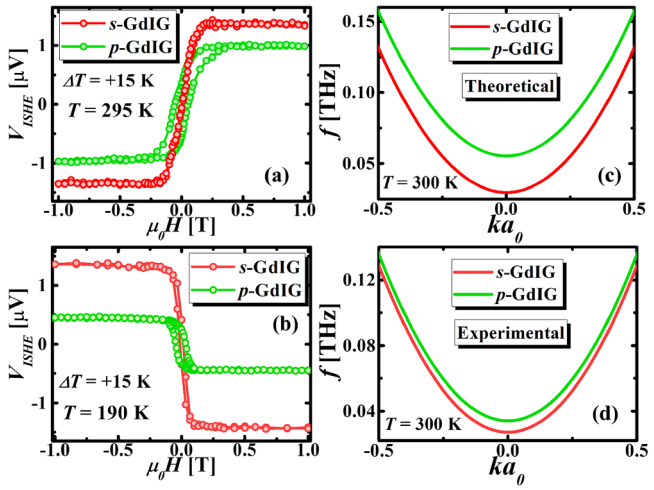

FIG. 8. Comparison of the $V_{\text{ISHE}}(H)$ hysteresis loops for the *p*-GdIG film and the *s*-GdIG film for $\Delta T = +15$ K at (a) $T = 295$ K and (b) $T = 190$ K. Comparison the magnon frequency dispersion for the *p*-GdIG and *s*-GdIG films at room temperature for $\mu_0 H = 1$ T for (c) theoretically and (d) experimentally estimated value of K_{eff}.

In this context, we would like to highlight that although the low-frequency sub-thermal magnons are primarily responsible for the long-range thermo-spin transport and therefore provide the major contribution toward the LSSE signal in thick films (with thickness of several micrometers) and bulk magnetic materials,[65–67] the contribution of the high energy thermal magnons toward the LSSE signal is significant in magnetic thin films.[68] The magnitude of the LSSE voltage decreases monotonically with reducing the thickness of the magnetic layer. Such thickness dependence of the LSSE signal indicates that the population of the thermally excited magnons which contribute toward the LSSE signal is limited by the boundary conditions. If the thickness of the magnetic layer is much higher than $\langle\xi\rangle$, the low-frequency sub-thermal magnons primarily contribute toward the long-range thermo-spin transport and hence the LSSE signal. However, if the thickness of the magnetic thin film is smaller than $\langle\xi\rangle$, the long-range low-frequency sub-thermal magnons cannot recognize the local temperature gradient and then, mostly the high-frequency thermal magnons contribute toward the LSSE signal.[68] It is important to note that for PLD-grown YIG thin films, $\langle\xi\rangle \approx 100$ nm, whereas for YIG slabs and thick YIG films, $\langle\xi\rangle$ varies between 1 and 5 μm.[31] Considering these facts, $\langle\xi\rangle \approx 45$ nm for the PLD-grown single-crystalline GdIG thin films is not unreasonable. Therefore, the high-frequency thermal magnons also play an important role in LSSE in magnetic thin films in addition to the low energy sub-thermal magnons with longer thermalization length. However, $\langle\xi\rangle$ for our *p*-GdIG film is definitely shorter than that of the single-crystalline GdIG films due to comparatively higher magnetic anisotropy of the *p*-GdIG film. Furthermore, it is known that V_{LSSE} is highly susceptible to the surface morphology[60,69] of the magnetic film as well as interfacial magnetic properties.[70,71] Therefore, the grain-boundary scattering in the *p*-GdIG film contributes significantly toward magnon scattering which causes spin-wave damping in *p*-GdIG and eventually influences spin-angular momentum transfer from the GdIG film to the Pt layer and thereby reduces the LSSE signal.[69,70,72] This explains lower value of V_{LSSE} in the *p*-GdIG film compared to the *s*-GdIG film.

To have a qualitative understanding of the origin of the lower LSSE signal in the *p*-GdIG film than in the *s*-GdIG film, we have estimated the magnon frequency dispersion for both *p*-GdIG and *s*-GdIG films at room temperature. Since $|V_{\text{LSSE}}|$ of GdIG is dominated by the β-mode within our measured temperature range,[24] we have considered a single magnon mode (β-mode) with parabolic band at room temperature. According to the classical Heisenberg model for spin waves in a magnetic material, the magnon frequency dispersion at low energies can be written as[63,66,68,73] $\hbar\omega_k = g_{\text{eff}}\mu_B H + D_{\text{SW}} \cdot k^2 a_0^2 + E_{\text{ani}}(K_{\text{eff}})$. Here, the first term is related to the Zeeman energy gap due to the application of external magnetic field (g_{eff} is the effective Landé g-factor and μ_B is the Bohr magneton), the second term represents the spin-wave stiffness (D_{SW} is the spin-wave stiffness constant and a_0 is the lattice constant), and the third term is associated with the contribution of effective magnetic anisotropy energy, $E_{\text{ani}}(K_{\text{eff}})$. Here, we have made an approximation that the value of D_{SW} for GdIG is approximately equal to that of YIG, i.e.,

$D_{SW}a_0^2 = 4.2 \times 10^{-29}$ erg · cm^2 at room temperature.[68] Using the expression, $K_{eff} = K_{shape} + K_{mc} + K_{me}$, we determined $E_{ani}(K_{eff})$ for both *p*-GdIG and *s*-GdIG films. Considering $M_S \approx 20$ kA/m at room temperature, $\lambda_{111} = -3.1 \times 10^{-6}$,[62] $a_{GSGG} = 12.57$ Å and $a_{GdIG} = 12.48$ Å, $Y = 2 \times 10^{10}$ N/m^2 and $\eta = 0.2$,[11,12] and $K_{mc} = 0.058$ kJ/m^3,[74] we obtain a theoretical value of $K_{eff} = +1.5$ kJ/m^3 for the *s*-GdIG film. However, the IP and OOP $M(H)$ hysteresis measurements presented in Fig. S2 in the supplementary material reveal $K_{eff} \approx +0.65$ kJ/m^3 for our *s*-GdIG film. On the other hand, the theoretically estimated values of K_{eff} for the *p*-GdIG film are +9.6 kJ/m^3. However, the IP and OOP $M(H)$ hysteresis measurements presented in Fig. 2(a) indicates an experimental value of $K_{eff} \approx +3$ kJ/m^3 for our *p*-GdIG film. As shown in Figs. 8(c) and 8(d), we have compared the magnon frequency dispersion for the *p*-GdIG and *s*-GdIG films at room temperature for $\mu_0 H = 1$ T for theoretically and experimentally estimated values of K_{eff}, respectively. It is evident that for both theoretical and experimental cases, the opening of the magnon energy gap for the *p*-GdIG film is higher than that for the *s*-GdIG film as $K_{eff}^{p\text{-GdIG}} > K_{eff}^{s\text{-GdIG}}$. The higher value of magnon energy gap in the *p*-GdIG film compared to the *s*-GdIG film thus indicates the higher possibility of freezing out of the low energy sub-thermal magnons in the *p*-GdIG film, which is responsible for the lower value of the LSSE voltage in the *p*-GdIG film compared to the *s*-GdIG film.

Furthermore, we would like to highlight that for more accurate estimation of the temperature dependence of S_{LSSE}, further measurement of the temperature dependence of κ_{GdIG}^{Poly} is required. Ideally, polycrystallinity increases phonon scattering at the grain boundaries which leads to reduced thermal conductivity in polycrystalline GdIG film compared to the single-crystalline GdIG film. In other words, since $\kappa_{GdIG}^{Poly} < \kappa_{GdIG}^{Single}$, higher value of $\Delta T_{eff} = \Delta T_{GdIG}$ is expected for the *p*-GdIG film compared to a single-crystalline GdIG film with similar thickness, which leads to reduction of S_{LSSE} in the *p*-GdIG film compared to its single-crystalline counterpart as $S_{LSSE} \propto 1/\Delta T_{eff}$. Since S_{LSSE} scales with the thermal conductivity,[60] the LSSE performance of the p-GdIG films can be improved by increasing κ_{GdIG}^{Poly}. Enhancement of κ_{GdIG}^{Poly} can be achieved by increasing the average grain size[75] of the *p*-GdIG films, which might be achieved by thermal annealing or, by interface engineering trough tuning of the growth and annealing protocol.

V. CONCLUSION

To summarize, we have observed PMA at room temperature in a 130 nm-thick polycrystalline GdIG film with $T_{Comp} \approx 240$ K grown on a Si/SiO$_2$ substrate. The magnetic easy axis reorients from the OOP to the IP direction below 180 K, similar to a 31 nm-thick single-crystalline GdIG film grown epitaxially on GSGG substrate that also showed PMA at room temperature. The LSSE voltage not only demonstrated a sign-inversion at T_{Comp}, but also showed noticeable changes around $T_S = 180$ K. The temperature-dependent SH-AHE results complement the noticeable changes observed in the LSSE signal of the polycrystalline GdIG film around T_{Comp} and T_S. However, $|V_{LSSE}|$ in the *p*-GdIG film is lower than for the *s*-GdIG film due to the grain-boundary-enhanced magnetic anisotropy and increased magnon scattering in the polycrystalline film. Our study will pave the way for further exploration of REIG-based highly efficient spincaloritronic devices grown on non-garnet substrates as well as provide a step toward the development of low-cost CMOS-compatible REIG-based systems with unconventional PMA for magnonic memory and information processing applications.

SUPPLEMENTARY MATERIAL

See the supplementary material for experimental details related to the structural and morphological characterizations, detailed magnetometry data, and the results of the LSSE measurements performed on the *s*-GdIG film.

ACKNOWLEDGMENTS

Financial support by the US Department of Energy, Office of Basic Energy Sciences, Division of Materials Science and Engineering under Award No. DE-FG02-07ER46438 at USF and by the German Research Foundation (DFG) within Project No. 318592081AL618/37-1 at U Augsburg are gratefully acknowledged.

AUTHOR DECLARATIONS

Conflict of Interest

The authors have no conflicts to disclose.

Author Contributions

Amit Chanda: Conceptualization (equal); Data curation (equal); Formal analysis (lead); Investigation (equal); Methodology (equal); Writing – original draft (lead). **Christian Holzmann:** Data curation (equal); Formal analysis (equal); Investigation (equal); Methodology (equal); Writing – review & editing (equal). **Noah Schulz:** Data curation (supporting); Formal analysis (supporting); Investigation (supporting); Writing – review & editing (supporting). **David Stein:** Data curation (supporting); Formal analysis (supporting); Investigation (supporting); Writing – review & editing (supporting). **Manfred Albrecht:** Conceptualization (equal); Funding acquisition (equal); Project administration (equal); Resources (equal); Supervision (equal); Validation (equal); Writing – review & editing (equal). **Manh-Huong Phan:** Funding acquisition (equal); Investigation (equal); Supervision (equal); Validation (equal); Writing – review & editing (equal). **Hariharan Srikanth:** Conceptualization (lead); Funding acquisition (lead); Investigation (equal); Project administration (lead); Resources (lead); Supervision (lead); Validation (lead); Writing – review & editing (lead).

DATA AVAILABILITY

The data that support the findings of this study are available from the corresponding authors upon reasonable request.

REFERENCES

[1] A. V. Chumak, V. I. Vasyuchka, A. A. Serga, and B. Hillebrands, "Magnon spintronics," Nat. Phys. **11**(6), 453–461 (2015).

[2]L. J. Cornelissen, J. Liu, R. A. Duine, J. Ben Youssef, and B. J. Van Wees, "Long-distance transport of magnon spin information in a magnetic insulator at room temperature," Nat. Phys. **11**(12), 1022–1026 (2015).
[3]M. Deb, E. Popova, M. Hehn, N. Keller, S. Mangin, and G. Malinowski, "Picosecond acoustic-excitation-driven ultrafast magnetization dynamics in dielectric Bi-substituted yttrium iron garnet," Phys. Rev. B **98**(17), 174407 (2018).
[4]M. Shalaby, F. Vidal, M. Peccianti, R. Morandotti, F. Enderli, T. Feurer, and B. D. Patterson, "Terahertz macrospin dynamics in insulating ferrimagnets," Phys. Rev. B **88**(14), 140301 (2013).
[5]Y. Sun, H. Chang, M. Kabatek, Y.-Y. Song, Z. Wang, M. Jantz, W. Schneider, M. Wu, E. Montoya, B. Kardasz *et al.*, "Damping in yttrium iron garnet nanoscale films capped by platinum," Phys. Rev. Lett. **111**(10), 106601 (2013).
[6]C. O. Avci, A. Quindeau, C.-F. Pai, M. Mann, L. Caretta, A. S. Tang, M. C. Onbasli, C. A. Ross, and G. S. D. Beach, "Current-induced switching in a magnetic insulator," Nat. Mater. **16**(3), 309–314 (2017).
[7]S. Emori, U. Bauer, S.-M. Ahn, E. Martinez, and G. S. D. Beach, "Current-driven dynamics of chiral ferromagnetic domain walls," Nat. Mater. **12**(7), 611–616 (2013).
[8]C. Holzmann, and M. Albrecht, "Iron garnet thin films for applications in magnonics and spintronics," in *Encyclopedia of Materials: Electronics* (Elsevier, Amsterdam, 2023) Vol. 1, pp. 777–795 (2023).
[9]A. Quindeau, C. O. Avci, W. Liu, C. Sun, M. Mann, A. S. Tang, M. C. Onbasli, D. Bono, P. M. Voyles, and Y. Xu, "$Tm_3Fe_5O_{12}$/Pt heterostructures with perpendicular magnetic anisotropy for spintronic applications," Adv. Electron. Mater. **3**(1), 1600376 (2017).
[10]E. R. Rosenberg, L. Beran, C. O. Avci, C. Zeledon, B. Song, C. Gonzalez-Fuentes, J. Mendil, P. Gambardella, M. Veis, C. Garcia *et al.*, "Magnetism and spin transport in rare-earth-rich epitaxial terbium and europium iron garnet films," Phys. Rev. Mater. **2**(9), 94405 (2018).
[11]S. M. Zanjani and M. C. Onbaşlı, "Predicting new iron garnet thin films with perpendicular magnetic anisotropy," J. Magn. Magn. Mater. **499**, 166108 (2020).
[12]C. Holzmann, A. Ullrich, O.-T. Ciubotariu, and M. Albrecht, "Stress-induced magnetic properties of gadolinium iron garnet nanoscale-thin films: Implications for spintronic devices," ACS Appl. Nano Mater. **5**(1), 1023–1033 (2022).
[13]J. Ding, C. Liu, Y. Zhang, U. Erugu, Z. Quan, R. Yu, E. McCollum, S. Mo, S. Yang, H. Ding *et al.*, "Nanometer-thick yttrium iron garnet films with perpendicular anisotropy and low damping," Phys. Rev. Appl. **14**(1), 14017 (2020).
[14]J. J. Bauer, E. R. Rosenberg, and C. A. Ross, "Perpendicular magnetic anisotropy and spin mixing conductance in polycrystalline europium iron garnet thin films," Appl. Phys. Lett. **114**(5), 052403 (2019).
[15]K. Srinivasan and B. J. H. Stadler, "Review of integrated magneto-optical isolators with rare-earth iron garnets for polarization diverse and magnet-free isolation in silicon photonics," Opt. Mater. Express **12**(2), 697–716 (2022).
[16]L. Sheng, J. Chen, H. Wang, and H. Yu, "Magnonics based on thin-film iron garnets," J. Phys. Soc. Jpn **90**(8), 81005 (2021).
[17]J. J. Bauer, E. R. Rosenberg, S. Kundu, K. A. Mkhoyan, P. Quarterman, A. J. Grutter, B. J. Kirby, J. A. Borchers, and C. A. Ross, "Dysprosium iron garnet thin films with perpendicular magnetic anisotropy on silicon," Adv. Electron. Mater. **6**(1), 1900820 (2020).
[18]E. Popova, N. Keller, F. Gendron, L. Thomas, M.-C. Brianso, M. Guyot, M. Tessier, and S. S. P. Parkin, "Perpendicular magnetic anisotropy in ultrathin yttrium iron garnet films prepared by pulsed laser deposition technique," J. Vac. Sci. Technol. A **19**(5), 2567–2570 (2001).
[19]Y. Kajiwara, K. Harii, S. Takahashi, J. Ohe, K. Uchida, M. Mizuguchi, H. Umezawa, H. Kawai, K. Ando, and K. Takanashi, "Transmission of electrical signals by spin-wave interconversion in a magnetic insulator," Nature **464**(7286), 262–266 (2010).
[20]S. Rumyantsev, M. Balinskiy, F. Kargar, A. Khitun, and A. A. Balandin, "The discrete noise of magnons," Appl. Phys. Lett. **114**(9), 090601 (2019).
[21]K. Uchida, H. Adachi, T. Ota, H. Nakayama, S. Maekawa, and E. Saitoh, "Observation of longitudinal spin-Seebeck effect in magnetic insulators," Appl. Phys. Lett. **97**(17), 172505 (2010).
[22]G. E. W. Bauer, E. Saitoh, and B. J. Van Wees, "Spin caloritronics," Nat. Mater. **11**(5), 391–399 (2012).
[23]E.-J. Guo, J. Cramer, A. Kehlberger, C. A. Ferguson, D. A. MacLaren, G. Jakob, and M. Kläui, "Influence of thickness and interface on the low-temperature enhancement of the spin Seebeck effect in YIG films," Phys. Rev. X **6**(3), 031012 (2016).
[24]S. Geprägs, A. Kehlberger, F. Della Coletta, Z. Qiu, E.-J. Guo, T. Schulz, C. Mix, S. Meyer, A. Kamra, and M. Althammer, "Origin of the spin Seebeck effect in compensated ferrimagnets," Nat. Commun. **7**(1), 10452 (2016).
[25]B. Yang, S. Y. Xia, H. Zhao, G. Liu, J. Du, K. Shen, Z. Qiu, and D. Wu, "Revealing thermally driven distortion of magnon dispersion by spin Seebeck effect in $Gd_3Fe_5O_{12}$," Phys. Rev. B **103**(5), 54411 (2021).
[26]Y. Li, D. Zheng, B. Fang, C. Liu, C. Zhang, A. Chen, Y. Ma, K. Shen, H. Liu, A. Manchon *et al.*, "Unconventional spin pumping and magnetic damping in an insulating compensated ferrimagnet," Adv. Mater. **34**(24), 2200019 (2022).
[27]A. Chanda, C. Holzmann, N. Schulz, J. Seyd, M. Albrecht, M.-H. Phan, and H. Srikanth, "Scaling of the thermally induced sign inversion of longitudinal spin Seebeck effect in a compensated ferrimagnet: Role of magnetic anisotropy," Adv. Funct. Mater. **32**(9), 2109170 (2022).
[28]J. Cramer, E.-J. Guo, S. Geprägs, A. Kehlberger, Y. P. Ivanov, K. Ganzhorn, F. Della Coletta, M. Althammer, H. Huebl, R. Gross *et al.*, "Magnon mode selective spin transport in compensated ferrimagnets," Nano Lett. **17**(6), 3334–3340 (2017).
[29]M. Kuila, Z. Hussain, and V. R. Reddy, "MOKE study of magnetic compensation in polycrystalline gadolinium iron garnet thin film," J. Magn. Magn. Mater. **473**, 458–463 (2019).
[30]E. Sawatzky and E. Kay, "Magnetic and structural properties of epitaxial and polycrystalline GdIG films prepared by rf sputtering," J. Appl. Phys. **42**(1), 367–375 (1971).
[31]A. Kehlberger, U. Ritzmann, D. Hinzke, E.-J. Guo, J. Cramer, G. Jakob, M. C. Onbasli, D. H. Kim, C. A. Ross, and M. B. Jungfleisch, "Length scale of the spin Seebeck effect," Phys. Rev. Lett. **115**(9), 96602 (2015).
[32]U. Ritzmann, D. Hinzke, and U. Nowak, "Propagation of thermally induced magnonic spin currents," Phys. Rev. B **89**(2), 24409 (2014).
[33]G. Venkat, T. A. Rose, C. D. W. Cox, G. B. G. Stenning, A. J. Caruana, and K. Morrison, "Spin Seebeck effect in polycrystalline yttrium iron garnet pellets prepared by the solid-state method," Europhys. Lett. **126**(3), 37001 (2019).
[34]P. Wongjom, R. Phatthanakun, and C. Ruttanapun, "The observation of spin Seebeck effect of hybrid structure in bulk sintering polycrystalline of yttrium iron oxide ($Y_3Fe_5O_{12}$)/Pt," Integr. Ferroelectr. **222**(1), 44–55 (2022).
[35]K. Yamada, Y. Kurokawa, K. Kogiso, H. Yuasa, and M. Shima, "Observation of longitudinal spin Seebeck voltage in YIG films chemically prepared by co-precipitation and spin coating," IEEE Trans. Magn. **55**(2), 4500104 (2019).
[36]A. Chanda, D. Rani, J. Nag, A. Alam, K. G. Suresh, M. H. Phan, and H. Srikanth, "Emergence of asymmetric skew-scattering dominated anomalous Nernst effect in the spin gapless semiconductors $Co_{1+x}Fe_{1-x}CrGa$," Phys. Rev. B **106**(13), 134416 (2022).
[37]O. Ciubotariu, A. Semisalova, K. Lenz, and M. Albrecht, "Strain-induced perpendicular magnetic anisotropy and Gilbert damping of Tm_3 Fe_5O_{12} thin films," Sci. Rep. **9**(1), 17474 (2019).
[38]S. Geller, G. P. Espinosa, and P. B. Crandall, "Thermal expansion of yttrium and gadolinium iron, gallium and aluminum garnets," J. Appl. Crystallogr. **2**(2), 86–88 (1969).
[39]M. Daniel, M. Friedemann, N. Jöhrmann, A. Liebig, J. Donges, M. Hietschold, G. Beddies, and M. Albrecht, "Influence of the substrate thermal expansion coefficient on the morphology and elastic stress of $CoSb_3$ thin films," Phys. Status Solidi **210**(1), 140–146 (2013).
[40]Y.-T. Chen, S. Takahashi, H. Nakayama, M. Althammer, S. T. B. Goennenwein, E. Saitoh, and G. E. W. Bauer, "Theory of spin Hall magnetoresistance," Phys. Rev. B **87**(14), 144411 (2013).
[41]H. Nakayama, M. Althammer, Y.-T. Chen, K. Uchida, Y. Kajiwara, D. Kikuchi, T. Ohtani, S. Geprägs, M. Opel, S. Takahashi *et al.*, "Spin Hall magnetoresistance induced by a nonequilibrium proximity effect," Phys. Rev. Lett. **110**(20), 206601 (2013).

[42]Y. Li, D. Zheng, C. Liu, C. Zhang, B. Fang, A. Chen, Y. Ma, A. Manchon, and X. Zhang, "Current-induced magnetization switching across a nearly room-temperature compensation point in an insulating compensated ferrimagnet," ACS Nano **16**(5), 8181–8189 (2022).
[43]Q. Shao, A. Grutter, Y. Liu, G. Yu, C.-Y. Yang, D. A. Gilbert, E. Arenholz, P. Shafer, X. Che, C. Tang *et al.*, "Exploring interfacial exchange coupling and sublattice effect in heavy metal/ferrimagnetic insulator heterostructures using Hall measurements, x-ray magnetic circular dichroism, and neutron reflectometry," Phys. Rev. B **99**(10), 104401 (2019).
[44]Y. M. Lu, Y. Choi, C. M. Ortega, X. M. Cheng, J. W. Cai, S. Y. Huang, L. Sun, and C. L. Chien, "Pt magnetic polarization on $Y_3Fe_5O_{12}$ and magnetotransport characteristics," Phys. Rev. Lett. **110**(14), 147207 (2013).
[45]S. Meyer, R. Schlitz, S. Geprägs, M. Opel, H. Huebl, R. Gross, and S. T. B. Goennenwein, "Anomalous Hall effect in YIG| Pt bilayers," Appl. Phys. Lett. **106**(13), 132402 (2015).
[46]K. Oyanagi, J. M. Gomez-Perez, X.-P. Zhang, T. Kikkawa, Y. Chen, E. Sagasta, A. Chuvilin, L. E. Hueso, V. N. Golovach, F. S. Bergeret *et al.*, "Paramagnetic spin Hall magnetoresistance," Phys. Rev. B **104**(13), 134428 (2021).
[47]L. Liu, Z. Fan, Z. Chen, Z. Chen, Z. Ye, H. Zheng, Q. Zeng, W. Jia, S. Li, N. Wang *et al.*, "Spin-orbit torques in heavy metal/ferrimagnetic insulator bilayers near compensation," Appl. Phys. Lett. **119**(5), 52401 (2021).
[48]S. M. Rezende, R. L. Rodríguez-Suárez, R. O. Cunha, A. R. Rodrigues, F. L. A. Machado, G. A. F. Guerra, J. C. L. Ortiz, and A. Azevedo, "Magnon spin-current theory for the longitudinal spin-Seebeck effect," Phys. Rev. B **89**(1), 14416 (2014).
[49]J. Xiao, G. E. W. Bauer, K. Uchida, E. Saitoh, and S. Maekawa, "Theory of magnon-driven spin Seebeck effect," Phys. Rev. B **81**(21), 214418 (2010).
[50]M. Arana, M. Gamino, E. F. Silva, V. Barthem, D. Givord, A. Azevedo, and S. M. Rezende, "Spin to charge current conversion by the inverse spin Hall effect in the metallic antiferromagnet Mn_2Au at room temperature," Phys. Rev. B **98**(14), 144431 (2018).
[51]A. Azevedo, L. H. Vilela-Leão, R. L. Rodríguez-Suárez, A. F. L. Santos, and S. M. Rezende, "Spin pumping and anisotropic magnetoresistance voltages in magnetic bilayers: Theory and experiment," Phys. Rev. B **83**(14), 144402 (2011).
[52]S. Albarakati, W.-Q. Xie, C. Tan, G. Zheng, M. Algarni, J. Li, J. Partridge, M. J. S. Spencer, L. Farrar, Y. Xiong *et al.*, "Electric control of exchange bias effect in $FePS_3$–Fe_5GeTe_2 van der Waals heterostructures," Nano Lett. **22**(15), 6166–6172 (2022).
[53]R. Iguchi, K. Uchida, S. Daimon, and E. Saitoh, "Concomitant enhancement of the longitudinal spin Seebeck effect and the thermal conductivity in a Pt/YIG/Pt system at low temperatures," Phys. Rev. B **95**(17), 174401 (2017).
[54]P. Jiménez-Cavero, I. Lucas, D. Bugallo, C. López-Bueno, R. Ramos, P. A. Algarabel, M. R. Ibarra, F. Rivadulla, and L. Morellón, "Quantification of the interfacial and bulk contributions to the longitudinal spin Seebeck effect," Appl. Phys. Lett. **118**(9), 92404 (2021).
[55]A. De, A. Ghosh, R. Mandal, S. Ogale, and S. Nair, "Temperature dependence of the spin Seebeck effect in a mixed valent manganite," Phys. Rev. Lett. **124**(1), 17203 (2020).
[56]A. Prakash, B. Flebus, J. Brangham, F. Yang, Y. Tserkovnyak, and J. P. Heremans, "Evidence for the role of the magnon energy relaxation length in the spin Seebeck effect," Phys. Rev. B **97**(2), 20408 (2018).
[57]K. Uchida, T. Kikkawa, A. Miura, J. Shiomi, and E. Saitoh, "Quantitative temperature dependence of longitudinal spin Seebeck effect at high temperatures," Phys. Rev. X **4**(4), 041023 (2014).
[58]T. Ashworth, J. E. Loomer, and M. M. Kreitman, *Advances in Cryogenic Engineering* (Springer, 1973), pp. 271–279.
[59]C. J. Glassbrenner and G. A. Slack, "Thermal conductivity of silicon and germanium from 3 K to the melting point," Phys. Rev. **134**(4A), A1058 (1964).
[60]A. Miura, T. Kikkawa, R. Iguchi, K. Uchida, E. Saitoh, and J. Shiomi, "Probing length-scale separation of thermal and spin currents by nanostructuring YIG," Phys. Rev. Mater. **1**(1), 14601 (2017).
[61]R. F. Pearson, "Magnetocrystalline anisotropy of rare-earth iron garnets," J. Appl. Phys. **33**(3), 1236–1242 (1962).
[62]S. Iida, "Magnetostriction constants of rare earth iron garnets," J. Phys. Soc. Jpn **22**(5), 1201–1209 (1967).
[63]U. Ritzmann, D. Hinzke, A. Kehlberger, E.-J. Guo, M. Kläui, and U. Nowak, "Magnetic field control of the spin Seebeck effect," Phys. Rev. B **92**(17), 174411 (2015).
[64]A. Chanda, N. Schulz, C. Holzmann, J. Seyd, M. Albrecht, M.-H. Phan, and H. Srikanth, "Thermal generation of spin current and magnon propagation length in compensated ferrimagnetic $Gd_3Fe_5O_{12}$ thin films," IEEE Trans. Magn. **58**, 1500505 (2022).
[65]J. M. Gomez-Perez, S. Vélez, L. E. Hueso, and F. Casanova, "Differences in the magnon diffusion length for electrically and thermally driven magnon currents in $Y_3Fe_5O_{12}$," Phys. Rev. B **101**(18), 184420 (2020).
[66]H. Jin, S. R. Boona, Z. Yang, R. C. Myers, and J. P. Heremans, "Effect of the magnon dispersion on the longitudinal spin Seebeck effect in yttrium iron garnets," Phys. Rev. B **92**(5), 54436 (2015).
[67]J. S. Jamison, Z. Yang, B. L. Giles, J. T. Brangham, G. Wu, P. C. Hammel, F. Yang, and R. C. Myers, "Long lifetime of thermally excited magnons in bulk yttrium iron garnet," Phys. Rev. B **100**(13), 134402 (2019).
[68]T. Kikkawa, K. Uchida, S. Daimon, Z. Qiu, Y. Shiomi, and E. Saitoh, "Critical suppression of spin Seebeck effect by magnetic fields," Phys. Rev. B **92**(6), 64413 (2015).
[69]M. Kim, S. J. Park, and H. Jin, "Enhancing the spin Seebeck effect by controlling interface condition in Pt/polycrystalline nickel ferrite slabs," J. Appl. Phys. **127**(8), 85105 (2020).
[70]J. D. Arboleda, O. Arnache Olmos, M. H. Aguirre, R. Ramos, A. Anadon, and M. R. Ibarra, "Spin Seebeck effect in a weak ferromagnet," Appl. Phys. Lett. **108**(23), 232401 (2016).
[71]A. Chanda, D. DeTellem, Y. T. Hai Pham, J. E. Shoup, A. T. Duong, R. Das, S. Cho, D. V. Voronine, M. T. Trinh, D. A. Arena *et al.*, "Spin Seebeck effect in iron oxide thin films: Effects of phase transition, phase coexistence, and surface magnetism," ACS Appl. Mater. Interfaces **14**(11), 13468–13479 (2022).
[72]M. Y. Kim, S. J. Park, G.-Y. Kim, S.-Y. Choi, and H. Jin, "Designing efficient spin Seebeck-based thermoelectric devices via simultaneous optimization of bulk and interface properties," Energy Environ. Sci. **14**(6), 3480–3491 (2021).
[73]S. Shamoto, Y. Yasui, M. Matsuura, M. Akatsu, Y. Kobayashi, Y. Nemoto, and J. Ieda, "Ultralow-energy magnon anomaly in yttrium iron garnet," Phys. Rev. Res. **2**(3), 33235 (2020).
[74]E. R. Rosenberg, K. Litzius, J. M. Shaw, G. A. Riley, G. S. D. Beach, H. T. Nembach, and C. A. Ross, "Magnetic properties and growth-induced anisotropy in yttrium thulium iron garnet thin films," Adv. Electron. Mater. **7**(10), 2100452 (2021).
[75]B. Jugdersuren, B. T. Kearney, J. C. Culbertson, C. N. Chervin, M. B. Katz, R. M. Stroud, and X. Liu, "The effect of ultrasmall grain sizes on the thermal conductivity of nanocrystalline silicon thin films," Commun. Phys. **4**(1), 169 (2021).